

# PHENOMENOLOGY OF BANE BERRY NUCLEAR EVENT REVISITED WITH 3-D FINITE ELEMENT TRANSIENT SIMULATION

REACTOR SAFETY

**KEYWORDS:** *transient numerical simulation, finite element, underground nuclear explosion*

RAJEEV RANJAN, R. K. SINGH,\* S. K. SIKKA, and ANIL KAKODKAR  
*Bhabha Atomic Research Centre, Trombay, Mumbai 400 085, India*

Received May 15, 2002

Accepted for Publication May 23, 2005

*This paper highlights a three-dimensional (3-D) transient numerical simulation of the Baneberry event of December 18, 1970, with a 10-kT yield and a 278-m source depth, conducted at the Nevada Test Site. This site has complex geological features with preexisting faults and layered geological strata characterized by a hard Paleozoic layer below the source, and saturated tuff on the west side of the source and clay-rich tuff toward the east side, both overlaid by top alluvial layers. In addition, a layer of 50% montmorillonite is sandwiched between two layers of 20% montmorillonite on the east end. This event is reported to have vented because of fault rupture and shock-wave reflections from a closer hard Paleozoic layer near the source. Here, the shock-induced slip along the preexisting fault plane has an important bearing on the containment efficiency of this event. None of the earlier reported simulation studies address the above slip phe-*

*nomenon and the influence of variation in geological strata in the presence of the preexisting fault in a 3-D framework for underground nuclear events. The paper describes the capabilities of the SHOCK-3D finite element code for simulating short-time shock-wave propagation, fault rupture leading to sliding along the fault plane, and subsequent crater formation at ground zero with a long-duration transient computation to study the quasi-static behavior of the Baneberry event. Precise modeling schemes of the composite geological strata and fault system demonstrate that a dip-slip mechanism had developed for this event, leading to final venting. The present numerical computation results with SHOCK-3D are in excellent agreement with site observations. In addition, the limitations of earlier reported simulation results from the TENSOR two-dimensional axisymmetric code presented by Terhune et al. have also been overcome.*

## I. INTRODUCTION

This paper describes a methodology that uses the three-dimensional (3-D) finite element method (FEM) code SHOCK-3D for the numerical simulation of underground nuclear explosion (UNE) events for short-duration shock-wave propagation and long-duration dynamic and quasi-static responses of the layered media in the near-field region. It is important to model the shock-induced inelastic and hydrodynamic behavior of the geological media made of layers with different impedances to pick up the shock-wave reflections and transmissions from the layer interfaces and the free surface at ground zero (GZ) to account for the energy partitioning and related phenomena of mound formation, spallation, and surface

cratering. Further, the FEM-based computations can be used for investigation and assessment of various cases of containment efficiency of the host rock mass and wave propagation in the near field in the presence of large discontinuities, namely, faults and shear zones and vis-à-vis seismic response on a regional/global scale.

In the present work, 3-D transient finite element simulation using SHOCK-3D has been carried out for the 10-kT-yield Baneberry event of December 18, 1970, conducted at the Nevada Test Site. All the field and postshot observations as well as calculations of the cavity growth, mound formation, cratering, and other aspects of the close in-ground motion pertaining to this event from an axisymmetric numerical analysis reported earlier by Terhune et al.<sup>1,2</sup> have been successfully simulated with excellent accuracy in a 3-D framework. The Baneberry event with a 278-m shot depth and a 10-kT yield has a

\*E-mail: rksingh@magnum.barc.ernet.in

scaled depth of burial (SDOB) of  $129.3 \text{ m/kT}^{1/3}$ , and it should have been a fully contained explosion. However, it vented because of a fracture path owing to the presence of the Baneberry fault, dipping 59 to 68 deg  $\sim 45 \text{ m}$  from the source, in a layered system of Paleozoic, tuff, and alluvium rock strata. This hard Paleozoic rock beneath a partially saturated tuff medium on the west side was located closer to the source (within 80 to 90 m) because of tectonic displacement induced in the past by the pre-existing fault system. Basically, the emplacement of the source in the weaker tuffaceous medium (50% montmorillonite) with the main Baneberry fault and top alluvial cover and strong reflections from the near-source Paleozoic medium on the west side resulted in sliding and rupturing up to the free surface leading to venting.

Terhune et al.'s<sup>1,2</sup> two-dimensional (2-D) axisymmetric simulation presents a simplified analysis approach with two models of the layered geological system, designated BANE 1 and BANE 2. This approach was necessary because of limitations of the 2-D axisymmetric formulation of Schatz's TENSOR code.<sup>3</sup> BANE 1 simulates the event with the fault system (in fact an axisymmetric fault cone frustum) and represents the geological cross section west of the source, while BANE 2 represents the eastern geological cross section without any fault system. The transient calculations have been carried out with Schatz's TENSOR code<sup>3</sup> for 1-s duration, and the results have been supplemented with field observations and postshot measurements. These two computational models simulate most of the observable features such as cavity growth, free-surface reflections, mound growth, containment cage formation near the emplacement in the BANE 2 model, and fault rupture in the BANE 1 model and adequately explain the failure mechanism. However, the interaction between the partially saturated tuff layer on the west end with the 50% montmorillonite clay-rich tuff strata on the east end is not simulated. The papers by Terhune et al.<sup>1,2</sup> present the above two limiting cases, and interpretations for the failure mechanism have been deduced by overlapping these two sets of results. Further, the reported short-time transient analysis does not capture the complete sequence of events leading to venting and crater formation as observed on site.

The objective of the current paper is to present a 3-D simulation of the Baneberry event and explain the sequence of events that led to venting. The 3-D simulation results obtained with this analysis clearly demonstrate the interaction between partially saturated tuff on the west end of the emplacement and relatively weaker layers of tuff with 50% montmorillonite on the east end. These two rock strata are separated by the fault, and the relative movement of rock mass along the fault was supported in this configuration. In addition, the strong shock wave reflected from the hard Paleozoic layer located relatively closer to the source on the west end further enhanced this slip movement along the fault. This complex

3-D failure mechanism is precisely modeled in this paper, and the present study improves interpretation of the observed venting. Terhune et al.'s simplified axisymmetric simulation<sup>1,2</sup> presents a simplified view of the venting mechanism due to the inherent limitations of the TENSOR code with which results were obtained with the above-mentioned 2-D models as the limiting cases for two different axisymmetric simplified models.

In our study, a complete 3-D finite element analysis is presented for the Baneberry event by accounting for the semi-infinite layered media on the east and west sides of the source in an integrated 3-D half-symmetrical model. Thus, the important features of interlayer and free-surface interactions and, more importantly, the explosion-induced rupture and sliding along the fault plane are demonstrated with our SHOCK-3D code. The sliding along the fault plane and the resulting vent path are attributed to formation of a dip-slip mechanism due to a relatively stronger tuff medium overlying a high-impedance closer-to-the source Paleozoic stratum on the west end and a weaker clay-rich medium on a relatively distant (from the source) Paleozoic layer on the east end. In addition to the prediction of short- and long-time transient phenomena of the event, the predicted crater depth with a quasi-static analysis is found to be in close agreement with the field observations. Here, it has been possible to analyze the problem for a much longer duration using a nonreflecting boundary condition applied at the surfaces that are beyond the elastic radius from the source. This simulation thus avoids any spurious reflection from the numerical model boundary. Also, the influence of gravity is accounted to estimate the mound fallback-induced impact or slapdown effects of the spalled rock layers. This way we have been able to simulate all the features observed during the Baneberry event and explain more explicitly the sequence of events that led to venting.

The important inputs to analyze this class of problems are the source strength, dynamic rock properties, constitutive behavior, and Hugoniot equation of state for different rock layers. Table I describes the Baneberry site-specific physical and constitutive properties of the rock media that have been used for the present analysis. More details on the hydrodynamic Hugoniot equation of state and strength variation with confinement pressure are given in the paper by Terhune et al.<sup>1</sup>

A short transient computation of 200-ms duration for the Baneberry event is carried out to study the resulting cavity growth, shock-wave reflections from the free surface, and other interfaces of different rock strata. Further, a long transient computation of 8-s duration is carried out for the event to study the failure of the containment cage near the fault on the west end, rupture and sliding along the fault, and mound growth and its free fall due to the gravity effect.

It is shown that on the west end the tensile failure in the spalled degraded alluvial (Alluvium2) region around

TABLE I  
Physical Properties of Rock Media at Baneberry Site\*

Properties	Paleozoic Rock	20% Montmorillonite	Tuff 50% Montmorillonite	Partially Saturated Tuff	Alluvium	Degraded Alluvium
Bulk density (kg/m <sup>3</sup> )	2700	2140	2000	2000	2150	1940
Grain density (kg/m <sup>3</sup> )	2800	2650	2780	2600	2670	2640
Poisson's ratio	0.45	0.25	0.42	0.3	0.2	0.2
P-wave velocity (m/s)	6000	1834	1898	1950	1053	1710
Uniaxial compressive strength (MPa)	60.0	7.0	1.0	11	11	11
Shear strength (MPa)	75.0	4.2	2	7	8.3	8.3
Porosity (%)	0	6	0	2	9	17

\*Reference 1.

the fault is of significant magnitude, which also extends closer to the cavity compared to the east-side spalled alluvial region. Moreover, the compressive mean stress or pressure is shown to be significantly lower on the west end near the fault compared to the east end, which led to the containment cage failure on the west end. The crack profile due to the explosion near GZ is predicted and is found to be consistent with that observed in the reported postshot examinations by Terhune et al.<sup>1,2</sup> Finally, as a limiting case a transient simulation up to 13 s is carried out in a quasi-static manner with the assumption of free sliding along the fault plane, and the venting is postulated above the fault at a radial distance of 97 m southwest of GZ with uplift of the top alluvial strata. This approximate prediction obtained as a limiting case to capture the vent position is consistent with the observed vent location at a radial distance of 90 m toward the southwest direction from GZ.

This limiting case of sliding interface simulation with a relatively weaker shear layer within the fault finally predicts the subsidence crater shape and size, which is 25 to 26 m deep with a diameter of 200 m compared to the observed crater depth of 24 m and the subsidence zone of 128 m. The Baneberry event has been reported to vent after 3.5 min, and the crater formation was observed after ~16 min of the event. This is due to the long time required for the cavity gases to either cool or leak in the pores, leading to depressurization of the cavity. The present numerical prediction of the subsidence crater is achieved in an approximate quasi-static manner where in the cavity, gas pressure is reduced after ~8 s artificially equal to the overburden pressure of ~5.881 MPa at the cavity level to arrive at the final quasi-static value. Thus, this simplified numerical simulation with our SHOCK-3D finite element code has been able to illustrate the crater profile and the vent location successfully.

## II. SHOCK-3D TRANSIENT 3-D FINITE ELEMENT CODE

The SHOCK-3D 3-D transient code is based on the coupled finite element formulation for geological media

and the fluid medium to represent the different rock formations and the gas cavity near the source, respectively. SHOCK-3D is an explicit, transient, 3-D Lagrangian finite element code for shock-wave propagation problems. This code is based on similar numerical schemes of Cherry and Petersen,<sup>4</sup> Schatz,<sup>3,5</sup> and Burton et al.<sup>6</sup> in the FEM framework for underground explosion simulation. The noteworthy features of this code are its coupled strain rate-dependent elasto-viscoplastic formulation for geological media and the hydrodynamic formulation to represent the gas cavity with an equation of state. For optimum computational efficiency and accuracy, eight node isoparametric brick elements with a  $2 \times 2 \times 2$  gauss point integration scheme and appropriate viscous dissipation for shock front smearing are used for both domains. The set of transient semidiscrete equation (1), resulting from finite element discretization, is solved with an explicit time integration scheme for both domains described as follows:

$$\mathbf{M}\mathbf{a}^t + \mathbf{C}\mathbf{v}^t + \mathbf{S}^t(\mathbf{d}^t) = \mathbf{F}^t, \quad (1)$$

where

$\mathbf{M}$  = diagonal mass matrix

$\mathbf{C}$  = damping matrix

$\mathbf{S}^t(\mathbf{d}^t), \mathbf{F}^t$  = internal and external force vectors, respectively

$\mathbf{a}^t, \mathbf{v}^t, \mathbf{d}^t$  = vectors that denote acceleration, velocity, and displacement vectors, respectively, at time  $t$  (denoted in the superscript).

The central difference time marching scheme with time step  $\Delta t$  is used to integrate the above set of equations as shown in Eqs. (2), (3), and (4).

The acceleration field  $\mathbf{a}^{t+\Delta t}$  is obtained as

$$\mathbf{a}^{t+\Delta t} = \mathbf{a}^t = \mathbf{M}^{-1} [\mathbf{F}^t - \mathbf{C}\mathbf{v}^t - \mathbf{S}^t(\mathbf{d}^t)]. \quad (2)$$

Further, the velocity field  $\mathbf{v}^{t+\Delta t}$  is obtained as

$$\mathbf{v}^{t+\Delta t} = \mathbf{v}^t + \mathbf{a}^{t+\Delta t} \Delta t . \quad (3)$$

The displacement field is finally obtained as

$$\mathbf{d}^{t+\Delta t} = \mathbf{d}^t + \mathbf{v}^{t+\Delta t} \Delta t . \quad (4)$$

The internal force vector  $\mathbf{S}^{t+\Delta t}(\mathbf{d}^{t+\Delta t})$  is updated from the internal stress field  $\boldsymbol{\sigma}^{t+\Delta t}$  over the model domain  $'\Omega$  for subsequent time-step computations as

$$\mathbf{S}^{t+\Delta t}(\mathbf{d}^{t+\Delta t}) = \int_{'\Omega} \mathbf{B}^T \boldsymbol{\sigma}^{t+\Delta t} d'\Omega . \quad (5)$$

The displacement and velocity fields updated by Eqs. (3) and (4) are used to obtain the strains and strain rates at the numerical integration gauss points. Finally, the internal stress field is incremented at each time step depending on the stress rate. It is correlated with the Jaumann stress rate, which in turn is strain rate dependent. The damping matrix  $\mathbf{C}$  is generated with the Sommerfeld<sup>7</sup> radiation condition to simulate a nonreflecting boundary as described in Zienkiewicz et al.<sup>8</sup> and Zienkiewicz and Taylor<sup>9</sup> to avoid any spurious reflection from the model boundary with normal and tangential directions as  $n$  and  $t$ , respectively, as follows:

$$\sigma_n = \rho c_b v_n \quad (6)$$

and

$$\sigma_t = \rho c_s v_t , \quad (7)$$

where

$\sigma_n, \sigma_t$  = normal and tangential stresses, respectively

$v_n, v_t$  = normal and tangential components of the particle velocity at the mesh boundary, respectively

$\rho$  = medium density

$c_b, c_s$  = body wave and shear wave velocities for the medium, respectively.

These conditions are applied sufficiently away from the source where plane elastic wave conditions exist, in which case the wave speeds are constant.

### II.A. Constitutive Model for the Gas Cavity

In the gas cavity, nonviscous hydrodynamic formulation-based fluid elements with limited overburden pressure are used to correlate the pressure  $p$  with volumetric strain  $\epsilon_v$  and specific energy  $E$ . A general form of this equation for the cavity gas is given as

$$p = a_1 + a_2(\epsilon_v) + a_3(\epsilon_v)^2 + a_4(\epsilon_v)^3 + [a_5 + a_6(\epsilon_v) + a_7(\epsilon_v)^2]E . \quad (8)$$

Equation (8) is used to input  $p$  as a polynomial function depending on the volumetric strain level. Thus, the ideal gas model; the iron gas model as given by Butkovich<sup>10,11</sup>; or any other suitable experimental model can be generated from Eq. (8). In the present study a simplified linearized form of Eq. (8) with Schatz's bubble gas cavity model<sup>5</sup> has been used.

### II.B. Constitutive Model for the Geological Media

The constitutive model of Hoek and Brown<sup>12</sup> for the rock layers is available in the code. This model accounts for the confinement effect on the rock strength. Damage mechanics-based failure models are used depending on the strain levels for brittle and ductile failures. The damage mechanics failure rules are based on an accumulated damage parameter and are suitable for crack profile mapping near the source.

The Hugoniot equation of state at high shock pressures (in the  $M$ -bar range) and hydrostatic data (in the  $K$ -bar range) for different rock media available for reported simulation studies similar to the Butkovich<sup>11</sup> and Burton et al.<sup>6</sup> studies has been used in the present code formulation. It may be noted that loading and unloading bulk moduli in the different regimes such as the mean pressures corresponding to the maximum tensile and compressive stresses of the rock medium at zero confinement describing the Hugoniot elastic limits, the hydrostatic pressure range, and the high-pressure shock range are suitably included.

The loading and unloading bulk moduli for the entire pressure range are evaluated for different rock media. It is assumed that in the loading stage the pores in the rock are filled up depending on the surrounding confinement generated due to pressure shock. In the unloading stage the volumetric strain corresponds to the ideal grain density, or it is between the ideal grain density and the bulk density, depending on the confinement level at the onset of unloading. This has been verified and confirmed by underground explosion simulation studies as reported by Butkovich.<sup>11</sup>

It has been observed that these data are very important for obtaining the correct energy distribution in the rock medium, and improved computation is possible if site-specific data are available for a range of pressure values. The equation of state for the rock media is given as

$$p = K(\epsilon_v) + \Gamma(\epsilon_v)E , \quad (9)$$

where

$p$  = hydrodynamic pressure

$K(\epsilon_v)$  = local bulk modulus, obtained from Hugoniot equation of state depending on the loading or unloading condition

$\epsilon_v$  = volumetric strain

$E$  = specific energy

$\Gamma$  = Gruneisen parameter, which allows dissipation of energy and is a function of volumetric strain.

### II.C. Strain Rate-Dependent Model of SHOCK-3D Finite Element Code

The strain rate-dependent model of SHOCK-3D uses the modified form of classical elasto-viscoplastic constitutive theory, which accounts for strain-rate sensitivity with allowance for progressive degradation of strength. This theoretical model is from Bicanic and Zienkiewicz<sup>13</sup> and Bicanic<sup>14</sup> based on the modified elasto-viscoplastic model of Perzyna.<sup>15</sup> The practical application of this theory has been demonstrated by Cervera et al.<sup>16,17</sup> in the case of concrete structures for transient dynamic and impact loads. In view of the limitations of the classical elasto-plastic and elasto-viscoplastic models to deal with rate- and history-dependent problems for transient shock and dynamic loadings, the visco-plastic strain rate is defined as a function of elastic strain/stress rate. In addition, the damage due to the viscoplastic flow is monitored with the help of a variable strength limit surface. The yield surface defines the onset of viscoplastic flow, and the strength limit surface defines the initiation of material degradation, and these are represented with the help of the first stress invariant and the second invariant of deviatoric stresses. Constant failure strain-based criteria are used in this model irrespective of the strain rate.

Sandler et al.<sup>18</sup> and Yamada and Abou-Sayeed<sup>19</sup> have described generalized plasticity formulations with a cap model for shock loading of geological materials; they have suggested that rate dependence and hardening/softening of the yield surface could be represented for finite strain problems involving the Jaumann stress rate. The application of the rate-dependent plasticity model based on the first stress invariant and the second deviatoric stress invariant coupled with the damage model is described for a practical application of wave propagation problems in rock media by Ma et al.,<sup>20</sup> where in the equivalent tensile strain is selected as the damage parameter. In SHOCK-3D the formulation has been cast within the framework of the modified viscoplastic formulation of Cervera et al.,<sup>16,17</sup> and a table lookup method is employed for the strain rate effect, which is obtained from the elastic strain rate. Thus, the present viscoplastic constitutive model of SHOCK-3D consists of all the important features of rate-dependent inelastic behavior along with the equation of state that characterize the rock behavior in the different regimes of shock loading.

### II.D. Overburden Simulation

The overburden simulation is important to accurately simulate the transient problem of an underground explosion event since the rising mound is finally settled

due to fallback induced by gravity forces. This feature is computed with the gravity link option of the code to simulate the initial stress field due to the overburden. In order to avoid the overburden-induced compression failure at larger depths, the pressure versus compressibility ( $\mu = \rho/\rho_0 - 1$ ) curves for the different rock layers of Terhune et al.<sup>1,2</sup> are used with a shift depending on the level of overburden as a function of depth to maintain constant strengths of different rock layers so that initial stresses do not cause failure or collapse at increasing depth.

### III. FINITE ELEMENT MODEL FOR BANE BERRY EVENT

This computational study of the Baneberry event uses two 3-D finite element models (using half-symmetry assumptions) with eight noded brick elements for the rock media and eight noded brick fluid elements for the cavity with bubble model. Both these models have the same layering pattern, which is fairly representative of the complex geology of the east-west cross section of the aforementioned site. Model 1 represents a fine grid with a nominal size of  $\sim 15$  m near the source, with an extent of 350 m toward the fault on the west side of the source and 205 m on the east side. Model 2 (Fig. 1) has a larger extent with a coarser grid with a nominal size of  $\sim 20$  m and includes a geological formation up to 517.5 m toward the fault on the west side of the source and 605 m on the east side. In both these models, the stronger Paleozoic rock is at a depth of  $\sim 85$  m below the source on the west side and at a depth of 170 m on the east side. On top of it extending up to a height of 170 m above the source is a partially saturated tuff layer on the west side and a 50% montmorillonite-rich tuff layer on the east side. In addition, on the east end the 50% montmorillonite layer is sandwiched between the two thin layers of 20% montmorillonite as shown in Fig. 1. Above these tuff layers are the two top alluvial covers (degraded alluvium and alluvium) up to GZ. The main Baneberry fault pattern included on the west side of both these models is  $\sim 45$  m from the source with an eastward dip of 68 deg near the surface and 59 deg near the source and intercepts the entire thickness of the partially saturated tuff layer with partial intrusion in the degraded alluvial layer.

Terhune et al.<sup>1</sup> reported that a second fault west of the Baneberry fault with less displacement was indicated during the postshot drilling. This discontinuity may behave as a joint, unlike the active Baneberry fault in the virgin condition of the tuff layers. Both models 1 and 2 use an initial cavity size of  $6.38 \times 6.38 \times 6.38$  m where a net energy of 10 kT is given as input in the bubble model using the linearized form of the gas equation of state described earlier to initiate the transient process, and the gravity link is also applied to simulate the overburden within 0.125 s, which simulates the gravity fallback of the rising mound after a few seconds.

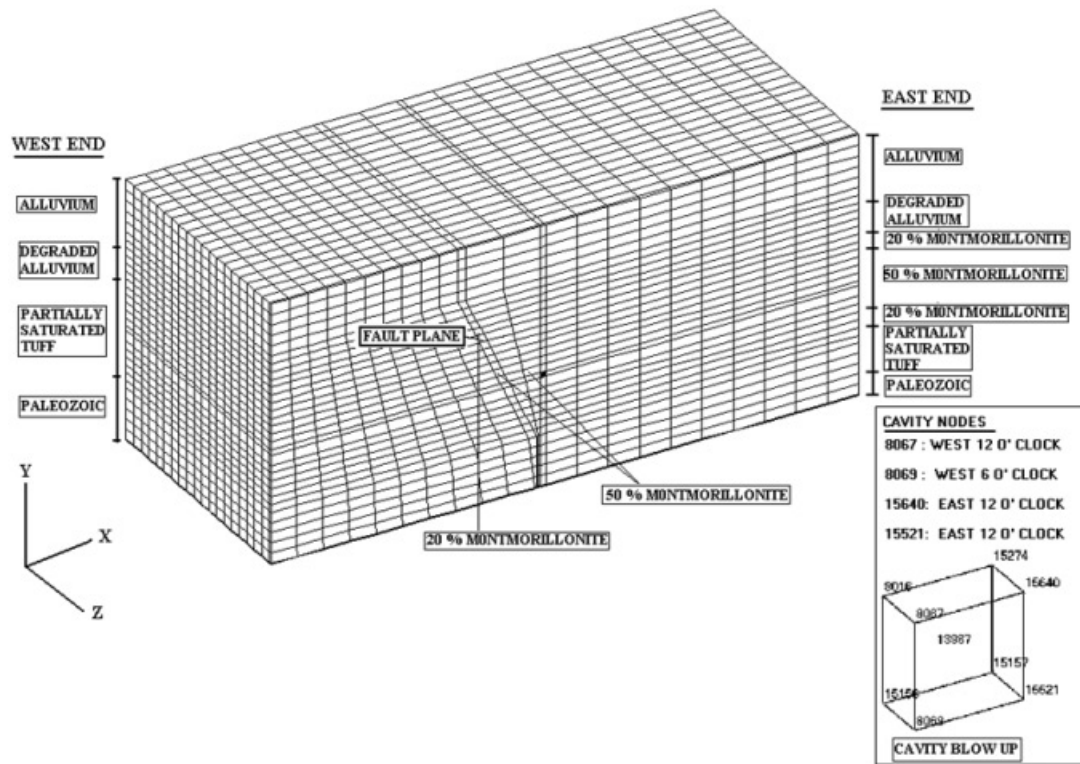


Fig. 1. The 3-D FEM half-symmetry model (northern quadrant) with layered rock media and fault for 10-kT Baneberry event. Location and nodal description of the source fluid element (emplacement cavity) are shown in an enlarged view.

Table I lists all the constitutive properties that have been used in the present analysis. More details on the Hugoniot pressure volume data and rock strength variation with confinement appear in the Terhune et al. paper.<sup>1</sup> These data sets were adopted in the present 3-D analysis in order to make a comparative study with the earlier simplified 2-D results and the site observations of Terhune et al.<sup>1,2</sup> In view of the complex geological formations near the Baneberry site and to account for the reported ambiguities in the in situ fault pattern (such as effectiveness of the reported second fault), the present simulation uses the following five cases with different fault/closely spaced weaker shear zone modeling schemes:

1. Model 1A includes the main Baneberry fault with an assumed trace length of 10 m simulated with weak clay layers. The weak shear zone thickness is assumed to be 8 m, as reported by Terhune et al.,<sup>1</sup> throughout the fault plane.

2. Model 1B includes the main Baneberry fault and the second minor fault both with a trace length of 10 m.

3. Models 2A and 2B are the same as models 1A and 1B, respectively, with the only difference being that the simulations are carried out on a coarser mesh to capture

a long-time transient response that necessitates models of a larger extent.

4. Model 3 is the same as model 2B with a fault trace length of 35 m transverse to the dip with weak shear layers.

5. Model 4 is the same as model 3 except that the weak shear zone allows sliding along the fault plane with almost negligible friction. In model 3, sliding along the fault plane is modeled with friction.

Models 1A and 1B with the limited extent have been used for short-duration transient computations up to 0.2 s with a view to capture the initial cavity growth and relevant near-source phenomena such as the extent of the plastic failure zone around the cavity, initiation of fault-cavity interactions, and reflections from hard Paleozoic layers on both sides of the source. Long-duration transient computations up to 8-s duration have been performed on models 2, 3, and 4 to capture the shock-induced fissuring and fracture path development along the fault plane up to the spall region of the top alluvial layer on the west side of the source. Attempts to use models 1A and 1B for long-duration transient computation were not successful because of their limited extent and because the elastic conditions at the nonreflecting

boundaries were violated. Thus, it was concluded that these local models are suitable only for short-duration transient simulation (within 0.2 s). In view of this, the short-time computations have also been performed on the models of larger extent (models 2, 3, and 4) to ensure the desired accuracy by comparing the results with model 1A and 1B results with a finer grid.

A few points are worth mentioning here. In all the 3-D models, we use half-symmetry, so the models simulate the northern quadrant of the Baneberry site. The nonreflecting boundary conditions [Eqs. (6) and (7)] are applied to the other side boundaries of the numerical model, and the top surface is kept free. This enables long-duration transient computation on a model with a finite boundary as mentioned earlier. In the reported 2-D axisymmetric model studies, Terhune et al.<sup>1,2</sup> use Paleozoic layers between the faults to reduce mesh distortion, while in actual geology the Paleozoic rock is below the fault. The fault system in our 3-D model is closely represented as observed in the postshot examinations. Further in the earlier axisymmetric model, the faults are represented as a conical frustum with the apex near the source and the base in the top alluvial layer. This limitation has also been overcome in our present 3-D model, and faults are represented as plane surfaces with a sliding interface. In the absence of definite data for the jointed rock mass along the strike of the fault, the above parametric models were used to investigate the cause of venting.

#### IV. COMPUTATIONAL RESULTS

In this section, the results of the all the analysis cases are presented in three parts, for both short- as well as long-duration transient simulation studies along with the containment cage evaluation for the Baneberry event. Here, inferences and comparisons based on Terhune et al.'s<sup>1,2</sup> earlier postshot investigations and calculations (up to 1-s duration) are also made.

#### IV.A. Short-Time Transient Computation up to 0.2 s

As indicated earlier, models 1A and 1B, with a finer mesh near the source, can support transient computation for a shorter duration because of the formation of inelastic zones near the nonreflecting boundary. Hence, these models more precisely capture the initial phenomena associated with cavity growth and initiation of the fault-cavity interaction. However, the analysis results for models 2A, 2B, 3, and 4 are also presented for the short-time duration for comparison with the finer-grid results of models 1A and 1B. The results presented in Tables II through VI give the cavity radius, maximum vertical velocity at GZ and 140 m above the source in the tuff medium close to the tuff-alluvial interface, and the maximum horizontal displacement and maximum resultant displacement at GZ.

The average cavity size is in the range of 34 to 35 m for models 1A and 1B, which is in agreement with Terhune et al.'s reported value<sup>1,2</sup> of 35 to 38 m. In Table II, resultant cavity displacements have been given for nodes 8067 and 8069 on the west side of the cavity and nodes 15640 and 15521 on the east side of the cavity (Fig. 1). For all the analysis cases, one may note that the west-side nodes located closer to the main Baneberry fault show a larger displacement value, thereby indicating the initial cavity interaction with the Baneberry fault. This also demonstrates that the plastic deformation zone around the cavity on the west side is close to the rupture zone initiated along the fault, which is unlike the deformation pattern of the east-side nodes.

A representative picture, Fig. 2, shows the cavity growth almost up to the fault boundary for model 1A at 0.2 s. Figures 3a and 3b present the vertical and resultant displacements, respectively, of four cavity nodes at the 12 and 6 o'clock positions on the west and east sides. The cavity sizes predicted by large models with coarser grids also show the average cavity size in the range of 38 to 40 m, which demonstrates that the selected coarser grid size is adequate for longer-duration transient computations without any significant compromise for near-source

TABLE II  
Maximum Cavity Node Displacement up to 0.2 s\*

Node / Position	Cavity Growth					
	Model 1A	Model 1B	Model 2A	Model 2B	Model 3	Model 4
8067 / 12 o'clock west	34.8	35.3	38.2	39.2	39.97	40.63
8069 / 6 o'clock west	33.7	38.8	43.9	45.2	46.15	48.48
15640 / 12 o'clock east	32.2	32.3	31.6	31.6	35.98	31.56
15521 / 6 o'clock east	36.2	35.3	35.9	39.2	39.97	35.98
Average cavity radius	34.2	35.4	38.2	38.8	40.5	39.2

\*In meters.

TABLE III  
Maximum Vertical Velocity up to 0.2 s at GZ\*

Time (s)	Y Velocity					
	Model 1A	Model 1B	Model 2A	Model 2B	Model 3	Model 4
0.01	5.74	5.74	5.74	5.74	4.7	5.74
0.05	4.6	4.7	4.2	4.7	5.99	4.7
0.1	4.8	4.82	4.96	4.95	4.74	4.73
0.15	7.45	7.4	7.4	7.6	7.51	7.4
0.2	6.5	6.72	6.0	5.72	5.99	6.0

\*In meters per second.

TABLE IV  
Maximum Vertical Velocity up to 0.2 s at 140 m Above the Working Point\*

Time (s)	Y Velocity					
	Model 1A	Model 1B	Model 2A	Model 2B	Model 3	Model 4
0.01	1.2	0.96	1.2	0.98	2.25	1.5
0.05	1.2	1.3	0.8	0.8	1.3	1.22
0.1	18.8	18.2	9.5	9.4	8.91	9.022
0.15	6.3	5.5	-6.3	-6.6	-6.46	-6.4
0.2	3.2	8.1	-13.5	-13.3	-13.5	-13.5

\*In meters per second.

TABLE V  
Maximum Total Displacement up to 0.2 s at GZ\*

Time (s)	Displacement					
	Model 1A	Model 1B	Model 2A	Model 2B	Model 3	Model 4
0.01	0.03	0.03	0.03	0.03	0.03	0.03
0.05	0.3	0.3	0.3	0.3	0.3	0.3
0.1	0.58	0.58	0.58	0.58	0.58	0.58
0.15	0.93	0.93	0.93	0.93	0.93	0.92
0.2	1.21	1.21	1.21	1.21	1.21	1.21

\*In meters.

modeling. The cavity sizes predicted by the different models are also influenced because of the different fault models used as a parametric case study. Hence, in view of the uncertainty of the fault pattern and the agreement with the reported cavity size of 37.2 m, the predictions are considered to be adequate for the present numerical study. As long as the total energy input to the initial cavity remains

constant (10 kT in the present case), the initial pressure would be governed by this energy, and with the bubble model used in the present computation, the results are unlikely to be significantly influenced a few cavity radii away from the working point as reported by Schatz.<sup>5</sup>

The displacements and velocities in the spall region at GZ and near the tuff-alluvial interface region,

TABLE VI  
Maximum Horizontal Displacement up to 0.2 s at GZ\*

Time (s)	X Displacement					
	Model 1A	Model 1B	Model 2A	Model 2B	Model 3	Model 4
0.01	0.0075	0.0067	0.0067	0.0067	0.0053	0.0067
0.05	0.058	0.049	0.049	0.049	0.041	0.049
0.1	0.18	0.15	0.15	0.15	0.13	0.15
0.15	0.27	0.27	0.26	0.27	0.22	0.27
0.2	0.35	0.38	0.37	0.38	0.35	0.38

\*In meters.

although very small for this short duration, compare well for all the models. The maximum particle velocity at GZ at 0.15 s is ~7.4 to 7.6 m/s and is ~5.7 to 6.7 m/s at 0.2 s for all the cases. This compares well with the site measurements of 6 m/s and the reported computational results in the range of 6.8 to 7.8 m/s. The maximum predicted particle velocity 140 m from the source is ~18.8 to 18.2 m/s for models 1A and 1B, respectively. These values are higher than the site observation and Terhune

et al.'s reported computational results,<sup>1,2</sup> which are in the range of 8 to 11 m/s.

Other models with a larger extent predict the velocity at the same elevation over the shot point in the range of 8.9 to 9.5 m/s in agreement with the reported value. The maximum particle velocities predicted by models 1A and 1B at later times (~0.2 s) are slightly higher because of the smaller extent and development of an inelastic zone at the nonreflecting boundary, so these

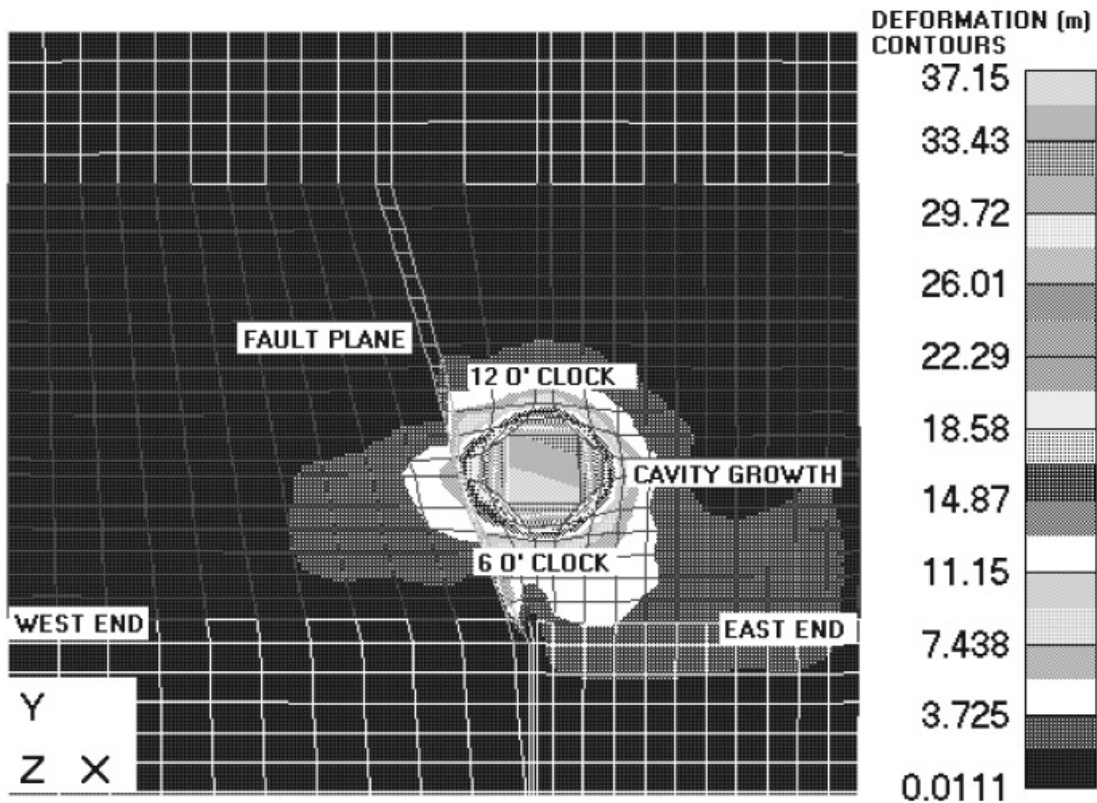


Fig. 2. Cavity growth (in meters) up to 0.2 s for model 1A.

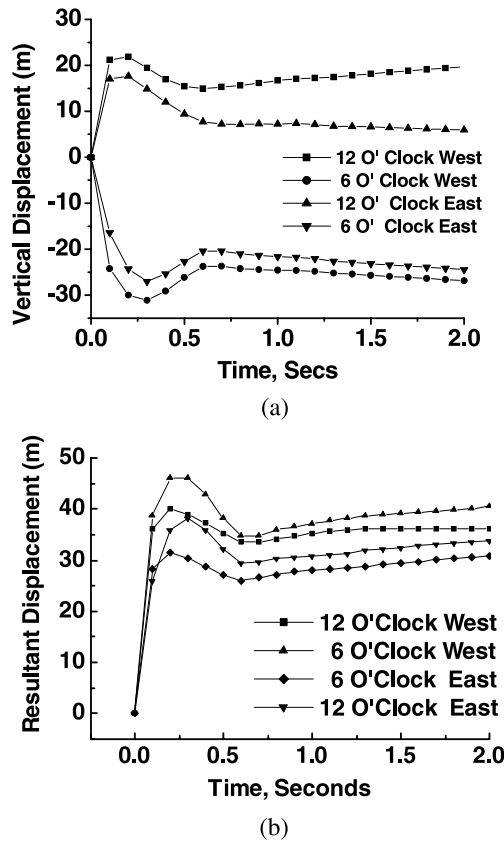


Fig. 3. For the four cavity nodes located on west and east sides of the cavity center (12 and 6 o'clock positions indicate top and bottom nodes, respectively) (in meters): (a) vertical displacement and (b) resultant displacement.

models are unsuitable for long-duration transient computations. Hence, we proceed with further analysis with models 2A, 2B, 3, and 4, which have a larger extent to ensure elastic conditions at the nonreflecting boundary, which is the necessary condition for wave propagation simulation studies.

It may be noted that in Table III the initial high velocity at 0.01 s near GZ in the range of 4.7 to 5.74 m/s is due to a computational artifact, since at this time the wave cannot arrive at GZ. This can be explained by Table V, wherein the corresponding maximum total displacement of ~0.03 m is uniformly predicted at GZ in all the models at 0.01 s. At this time, the maximum horizontal displacement is in the range of 0.0053 to 0.0075 m (Table VI). Thus, the maximum vertical displacement would be nearly 0.03 m at 0.01 s, which is insignificant compared to the displacement of 0.93 m observed at 0.15 s and 1.21 m at 0.2 s at which the wave actually arrives at GZ. This illustrates that the rock strengths and wave speeds are correctly simulated in the present numerical models. Accordingly, the peak velocity of 7.4 to 7.6 m/s at 0.15 s and the velocity in the range of 5.7 to 6.7 m/s at 0.20 s in Table III has been

observed for all the models. The high velocity of 5.7 m/s at 0.01 s is due to the gravity link applied for the overburden simulation in the initial part of the transient calculation up to 0.125 s and is a computational artifact. It takes some finite time for the gravity effects to reach the steady-state value. At later times, 0.15 to 0.2 s, the particle velocities of ~6.0 to 7.6 m/s are consistently predicted in agreement with the site observations.

IV.B. Long-Duration Transient Simulation

The results of cavity growth, the maximum vertical velocity, and displacement at GZ and at 140 m above the source in the tuff medium up to 8 s are presented in Tables VII through XI for all the cases, namely, models 2A, 2B, 3, and 4.

First, we discuss the computational results up to 2.0 s for different cases. The maximum vertical displacement at GZ up to 1 s is ~2.5 to 3.6 m, and the maximum horizontal displacement is ~0.8 to 0.9 m. The observed field spall-induced vertical displacement is ~1.8 m, and the reported value from the 2-D simulation is ~2.3 to 3.1 m, which compares well with the above computed value (~2.5 to 3.6 m) from SHOCK-3D. Similarly, the maximum reported horizontal displacement at GZ due to vent

TABLE VII

Maximum Horizontal Displacement up to 8.0 s at GZ\*

Time (s)	X Displacement			
	Model 2A	Model 2B	Model 3	Model 4
0.5	0.62	0.62	0.53	0.62
1.0	0.83	0.9	0.8	0.85
2.0	1.02	0.73	1.1	1.04
5.0	1.71	1.7	1.8	1.7
8.0	3.21	2.85	3.31	3.4

\*In meters.

TABLE VIII

Maximum Total Displacement up to 8.0 s at GZ\*

Time (s)	Displacement			
	Model 2A	Model 2B	Model 3	Model 4
0.5	2.6	2.6	2.7	2.67
1.0	3.6	3.6	3.5	3.5
2.0	3.7	3.7	3.9	3.7
5.0	23.11	20.3	22.6	22.7
8.0	34.98	30.7	33.6	35.0

\*In meters.

TABLE IX

Maximum Vertical Displacement up to 8.0 s at GZ\*

Time (s)	Y Displacement			
	Model 2A	Model 2B	Model 3	Model 4
0.5	2.69	2.63	2.63	2.65
1.0	3.6	3.6	3.45	2.47
2.0	-3.7	-3.7	-3.9	-3.6
5.0	-21.6	-20.3	-22.5	-22.7
8.0	-34.8	-30.6	-33.5	-35.0

\*In meters.

TABLE X

Maximum Vertical Velocity up to 8.0 s at 140 m Above the Working Point\*

Time (s)	Y Velocity			
	Model 2A	Model 2B	Model 3	Model 4
0.5	-15.0	-15.4	-15.3	-16.9
1.0	-3.95	-2.9	-4.4	-4.4
2.0	-3.38	-3.2	-4.4	-3.93
5.0	-3.56	-3.3	-3.8	-3.7
8.0	2.13	1.5	2.3	2.1

\*In meters per second.

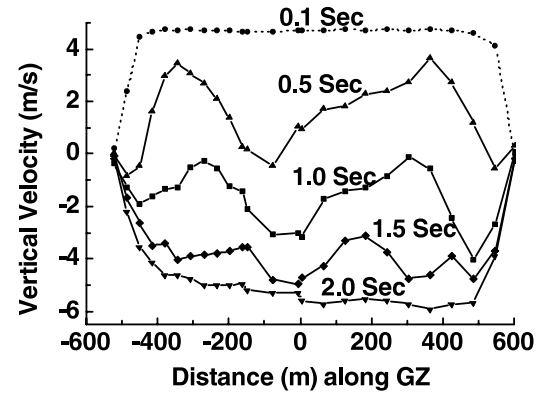
TABLE XI

Maximum Vertical Velocity up to 8.0 s at GZ\*

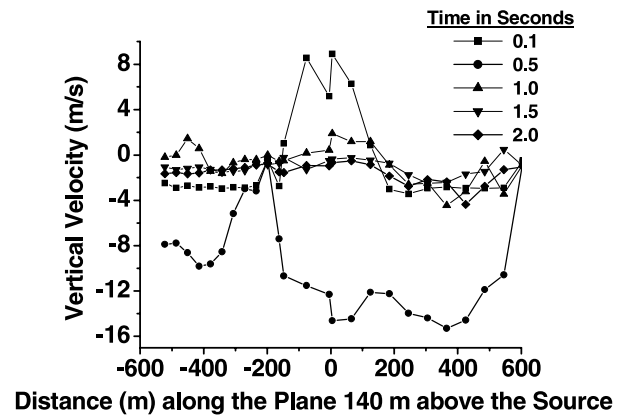
Time (s)	Y Velocity			
	Model 2A	Model 2B	Model 3	Model 4
0.5	3.8	3.97	3.6	3.66
1.0	-3.9	-3.82	-4.8	-4.8
2.0	-6.2	-5.99	-5.9	-5.8
5.0	-9.28	-8.26	-8.3	-9.0
8.0	-2.02	-1.83	2.1	-1.25

\*In meters per second.

fissure is 1 m, which is close to the present prediction (~0.8 to 0.9 m). Beyond this time, ~2 s, the spall-induced fallback and slapdown due to gravity become predominant, and the vertical displacement is in the range of -3.6 to -3.9 m. This is consistent with the vertical velocity variation as shown in Table XI, where the velocities become negative after 0.5 s. Figures 4a and 4b give the vertical velocity plots at GZ and the tuff-alluvial interface (140 m



(a)



(b)

Fig. 4. Vertical nodal velocity at 0.1, 0.5, 1.0, 1.5, and 2.0 s (in meters per second): (a) on the surface along GZ and (b) on the horizontal layer 140 m above the source.

above the source) for model 3 up to 2 s. Here, it is observed that near this interface, on the west end, the rate of fallback (vertical velocity approximately -10 m/s) is lower than that on the east end (vertical velocity approximately -15 m/s). This observation further supports the hypothesis that the cavity-fault interaction and spall induced in this region led to sliding along the fault plane, which caused venting on the west side of GZ. The shock reflection from the hard Paleozoic layer due to its closeness to the working point and the fault system on the west end further supported this slip movement.

As mentioned in Sec. IV.A, the gravity link is applied up to 0.125 s in these case studies also, and subsequently, the overburden stabilizes as an initial stress field. Hence, the initial high decelerations observed between 0.1 to 0.5 s in Figs. 4a and 4b are apparently due to numerical artifact. However, after stabilization of the overburden effect, the acceleration values are relatively smaller between 0.5 to 1.0 s and at subsequent times up to 2 s. Thus, the gravity link successfully simulates the mound fallback as illustrated in Figs. 4a and 4b. These

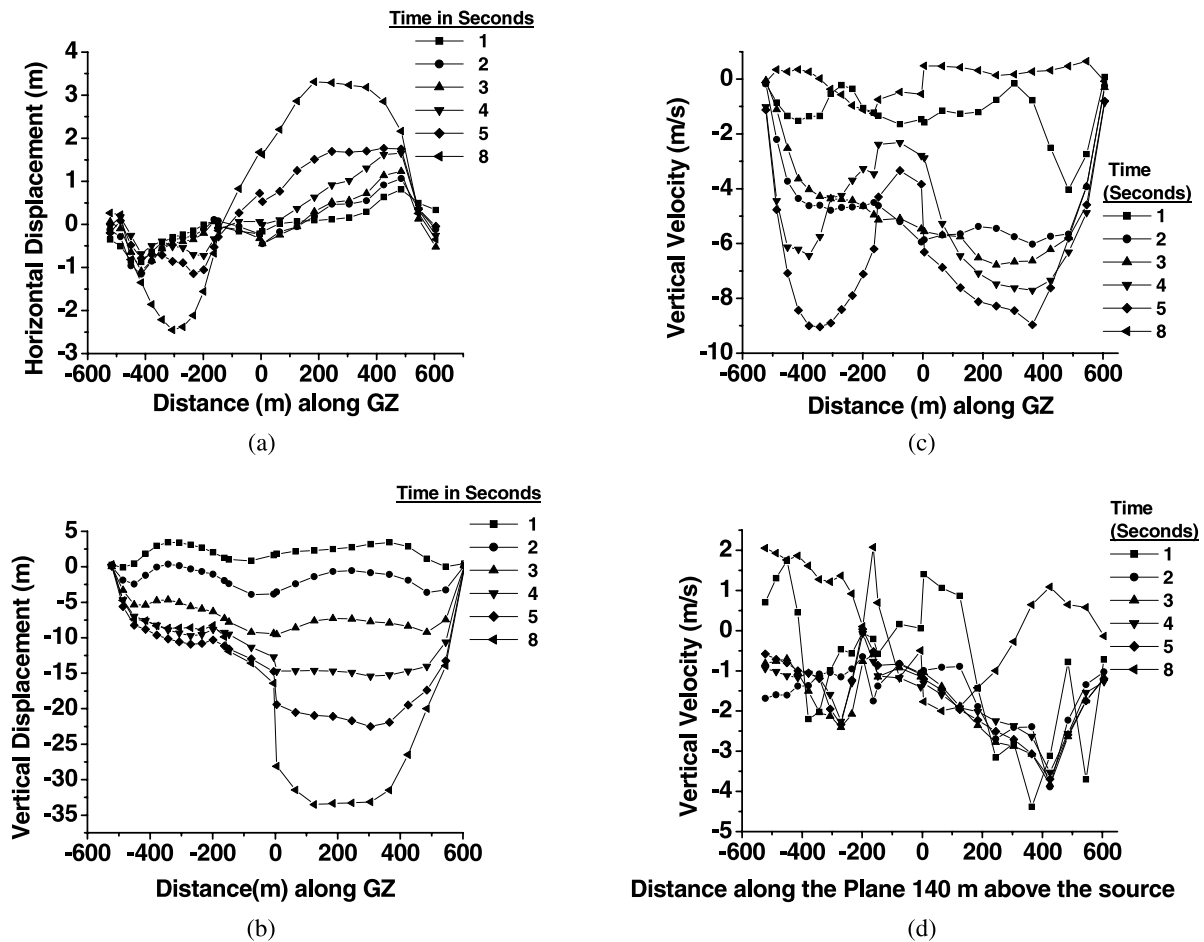


Fig. 5. At 1, 2, 3, 4, 5, and 8.0 s: (a) horizontal nodal displacement on the horizontal layer along GZ (top surface) for model 3 (in meters), (b) vertical nodal displacement on the horizontal layer 140 m above the source for model 3 (in meters), (c) vertical nodal velocity on the horizontal layer along GZ (top surface) for model 4 (in meters per second), and (d) vertical nodal velocity on the horizontal layer 140 m above the source for model 4 (in meters per second).

studies on the global models with different trace lengths of the single- and double-fault systems show uniform velocities consistent with the site observations. Further, it may be concluded from these parametric studies that although the presence of a single- or double-fault system resulted in the spall near the cavity and fault zone possibly due to cavity-fault interaction, this factor alone was not responsible for the observed venting. Terhune et al.<sup>1,2</sup> drew similar conclusions and also note that in the case of an earlier test closer to the Baneberry site, no venting was reported for such a highly scaled depth of burial. It was hence desirable to perform a quasi-static simulation to understand the vent mechanism and trace the crater profile; this numerical simulation is presented in Sec. IV.C.

#### IV.C. Predictions for Venting and Crater Formation

The transient computational results for a longer-duration event are further evaluated to identify the

rupture location resulting from sliding along the fault, the small mound growth, and its free fall due to the gravity effect.

Within 1 s, the sequence of events that follow indicate increased deformation, cracking in the fault region, and tuff-alluvium interface, which are a prelude to fissure development, venting, and crater formation in the vicinity of the free surface around GZ. Earlier reported studies by Terhune et al.<sup>1,2</sup> also concluded that containment cage failure took place within 1 s of the event because of a combination of three specific features of the Baneberry site, namely, the presence of the fault on the west end, clay-rich tuff material around the cavity on the east end, and stronger shock-wave reflections from the closer hard Paleozoic layer on the west end. This is presented in detail in Sec. IV.D. Here, we further continue to evaluate the results for longer duration up to 8 s to examine the influence of various fault systems on the displacement and velocity responses.

Figures 5a through 5d plot the horizontal displacement, vertical displacement, and vertical velocities at GZ and 140 m below GZ for models 3 and 4, respectively, up to 8 s. In the computations up to 8 s, the horizontal displacement at GZ is  $\sim 2.85$  to  $3.4$  m as given in Table VII for all the analysis cases in a region just above the fault protrusion in the top alluvial cover on the west side. The maximum vertical displacements are in the range of approximately  $-20$  to  $-23$  m at 5 s and approximately  $-30.5$  to  $-35$  m at 8 s as given in Table IX and occurs on the east side. Up to 8 s the radius of the zone of subsidence is  $>200$  m with an average depth of 25 m. This nonsteady subsidence marks the development of the final crater of dimensions comparable to the site observed subsidence crater of 24-m depth and 128-m diameter. The position of the crater is a few meters away from GZ toward the east side, and this shift from GZ can be attributed to the presence of the fault and accompanying explosion-induced sliding. This is further supported by strong reflections from the hard Paleozoic layer underlying the west-side tuff, 85 m below the source, with this effect being far less on the east side, which has the

Paleozoic layer at a larger depth of 170 m below the source in the numerical model, where the shock reflections were relatively weaker.

The maximum vertical velocity values reported in Table XI for the free surface are large, up to 5 s (approximately  $-8.3$  to  $-9.3$  m/s), after which at 8 s the top layer fallback is somewhat arrested (vertical velocity of approximately  $-1$  to  $-2$  m/s), and the rupture along the fault and the adjoining alluvial strata predominates. The maximum vertical velocity 140 m above the source near the tuff-alluvial interface at 5 s is approximately  $-3.3$  to  $-3.8$  m/s, after which at 8 s the maximum vertical velocity becomes positive ( $\sim 1.5$  to  $2.3$  m/s), and this occurs over the fault on the west side. This local free-surface effect centered over the fault indicates fracture path formation along the fault and heaving of the top alluvial cover around the fault and establishes the incipient venting phenomena. It may be noted that the displacement and velocity responses predicted by different models with various fault systems as shown in Tables VII through XI show comparable responses up to 8-s duration, which demonstrates that although the fault system

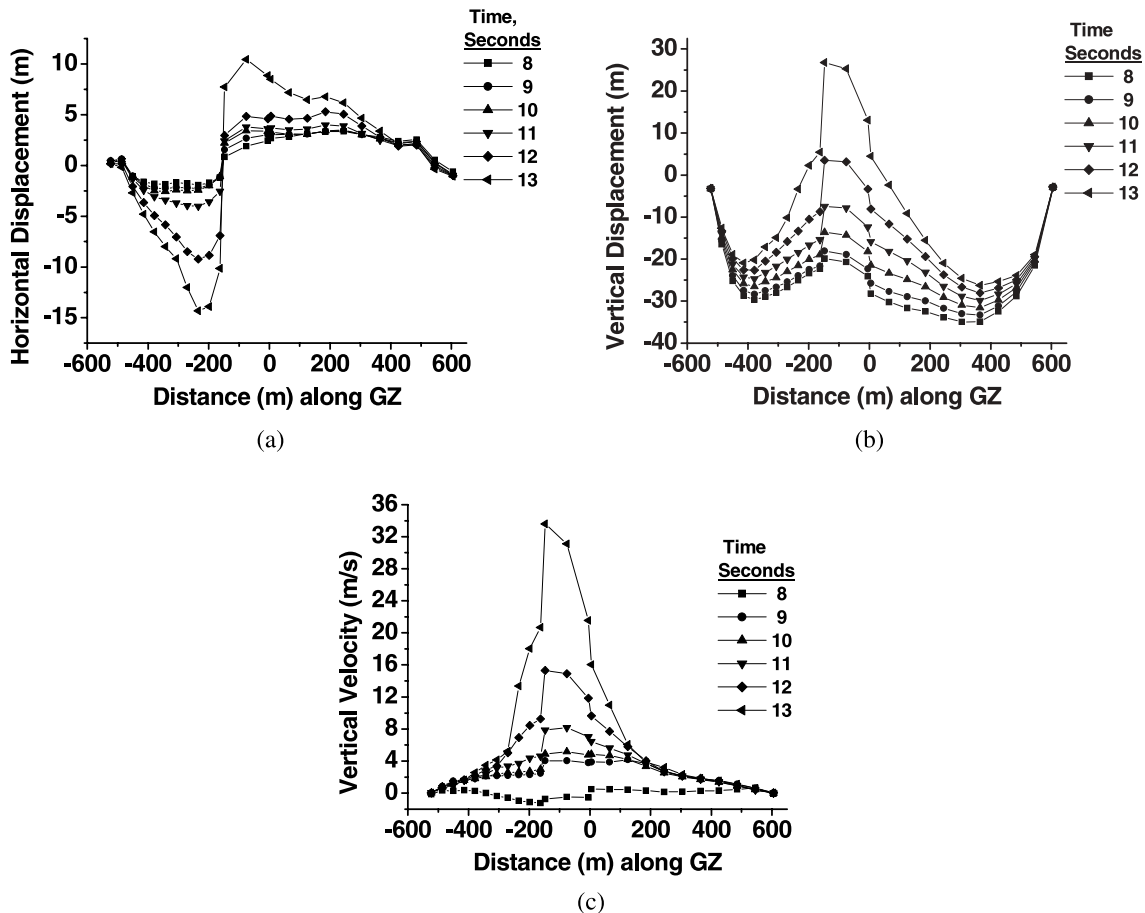


Fig. 6. At 8, 9, 10, 11, 12, and 13 s on the horizontal layer along GZ (top surface) for model 4: (a) horizontal nodal displacement (in meters), (b) vertical nodal displacement (in meters), and (c) vertical nodal velocity (in meters per second).

contributed to venting, it was not the only feature that caused venting, as confirmed by Terhune et al.'s results<sup>1,2</sup> also.

Further analysis was carried out for a longer duration up to 13 s to predict vent-induced uplift and subsidence crater formation. In this case study, model 4 has been used, which has a very weak shear layer, thus permitting free sliding along the fault plane. This was selected as a parametric case study to identify the vent location and the final crater shape as a limiting case. Normally, the subsidence crater formation takes a few tens of minutes to days and even weeks in some cases. In the case of the Baneberry event, the venting was reported after 3.5 min,

and the crater formation was observed after ~16 min of the event. After the event the cavity gases gradually cooled, and leakage through the pores initiated, both leading to depressurization of the cavity over a long period of time, which was followed by chimney collapse and crater formation. In the numerical transient analysis, the prediction of a subsidence crater is achieved in an approximate quasi-static manner, where the cavity gas pressure is gradually reduced after ~8 s, equal to the steady overburden pressure of ~5.881 MPa at the cavity elevation to trace the quasi-static configuration of the free surface. In the absence of the cavity pressure, the inelastic compressive stresses result in the instability-induced collapse

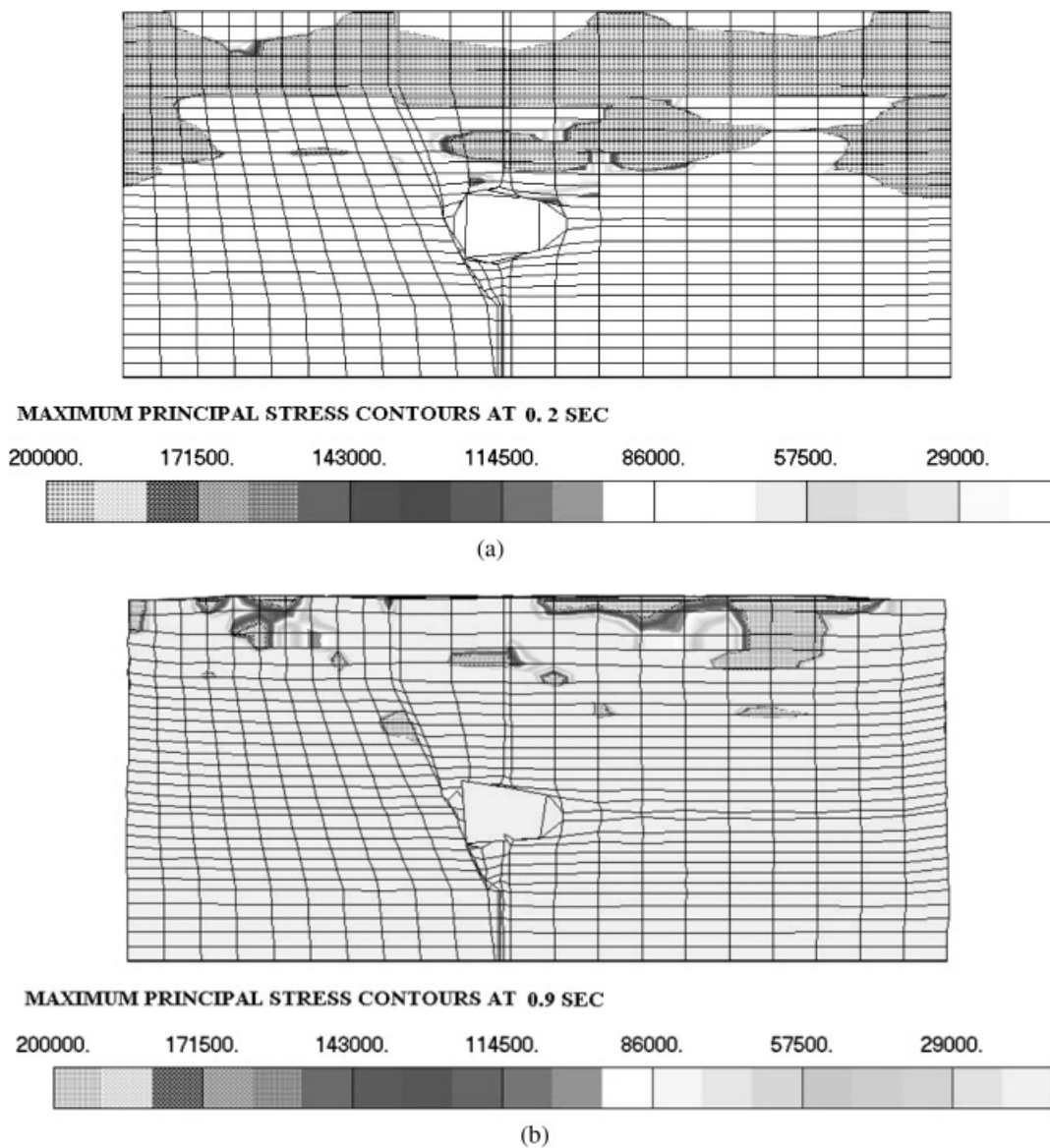


Fig. 7. Spall-induced tension failure shown with maximum principal tensile stress contours for model 3 (in newtons per square meters) at (a) 0.2 s, (b) 0.9 s, (c) 1.3 s, and (d) 2.0 s. (Figure continues on facing page.)

mechanism. The simplified numerical simulation scheme of SHOCK-3D has been successfully used to trace the crater profile and identify the vent location.

Figures 6a, 6b, and 6c show the vertical velocity and the vertical and horizontal displacement profiles up to 13 s obtained from the aforementioned quasi-static analysis on model 4. Here, the timescales are pseudo in nature as our principal objective is to arrive at the quasi-static final configuration of GZ. The increase in positive vertical velocity near the free surface over the fault after 8 s (Fig. 6c) indicates fissuring phenomena. Here, it can be seen that a local uplift of significant magnitude occurs on the free surface overlying the fault at a radial distance 97 m southwest of GZ due to sliding and final rupture of

the top alluvial layer. This prediction of vent location is consistent with the observed venting at a radial distance of 90 m toward the southwest direction from GZ. Also, the maximum horizontal displacement is  $\sim 8.5$  m on the free surface over the fault on the west end at 12 s as shown in Fig. 6a, which indicates the establishment of the vent path due to development of unstable rupturing. Although this maximum horizontal displacement is over-predicted with model 4 because of free sliding along the fault plane leading to final rupture at GZ, this quasi-static analysis has helped to locate the vent location in a qualitative manner consistent with the site observations. Moreover, the approximate crater profile (25- to 26-m crater depth with 200-m diameter) was also predicted, which

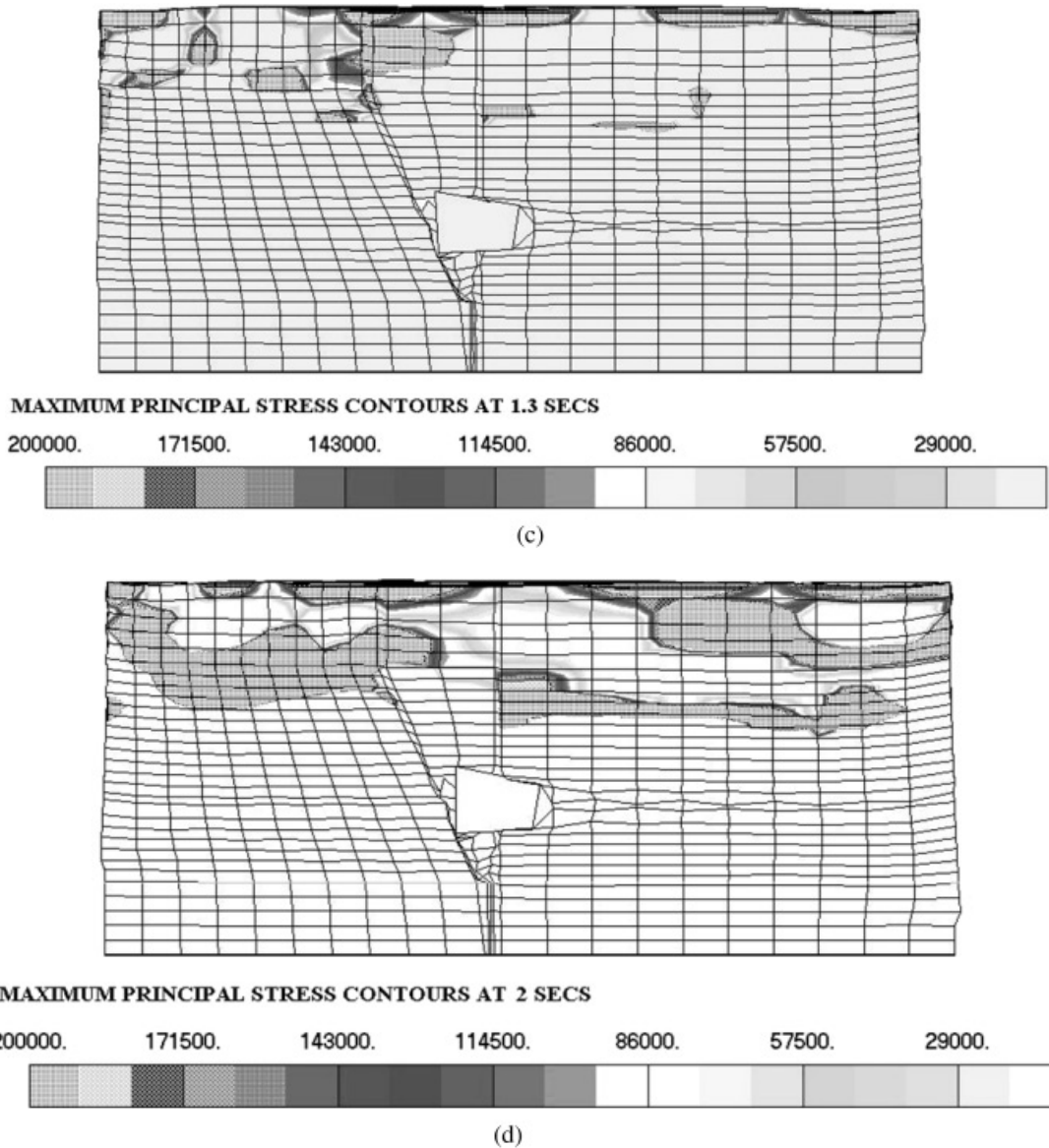


Fig. 7. Continued.

was observed at the site. Similar quasi-static analysis with model 3 showed a much reduced horizontal displacement of ~3.5 m and very small upheaving of the top alluvial layer on the west end, and it does not show the complete rupture of the top alluvial cover farther above the fault.

These quasi-static analyses confirm that the depressurization of the cavity, due to gradual leakage of the cavity gases through the cracks and pores as a result of cavity-fault interaction and the resultant spall very close to the cavity, caused collapse of the chimney, and the presence of the fault further supported sliding of the west-end rock mass along the slip plane. In the absence of details on the precise variation of the friction coefficient and the rock strength over different strata within the fault, the present analysis was carried out for the most severe case with model 4, where free sliding was permitted assuming a very weak shear layer. This, though, over-predicts the surface movements due to large rupture, but it appropriately explains the failure mechanism and vent location.

**IV.D. Stress and Strain Predictions for Containment Evaluation**

Now, we examine the stress and strain profiles near the cavity, around the fault plane and GZ for the Baneberry event to evaluate the containment behavior on the east and the west ends. Figures 7a through 7d show the maximum principal tensile stresses at 0.2, 0.9, 1.3, and 2 s, respectively, for model 3. The tensile stress band has

been specifically selected to examine the containment cage failure and leakage of the cavity gases through the rock pores and cracks that resulted in venting later, as mentioned in Sec. IV.C.

At 0.2 s (Fig. 7a), spall near the free surface and in the weak layers of the clay-rich tuff closer to the cavity is noted. The latter is due to the focusing of a shock wave induced by refraction with the presence of high-porosity degraded alluvium above the clay-rich tuff layer. Subsequently, spall in the fault plane closer to the cavity at 0.9 s (Fig. 7b) and heaving of the top surface on the west end due to shock-wave reflections from the hard Paleozoic layer underneath the working point are visible. This heaving of the top alluvial layer on the west end resulted in the rupture of the top alluvial cover, and the fault extended up to GZ at 1.3 s (Fig. 7c). It may be noted that in the virgin condition the top alluvial layer was without any fault, crack, or joint, but it was weakened because of focusing, strong shock-wave reflection from the Paleozoic layer on the west end, and the resultant sliding of the rock mass leading to upheaving. Further, more rupture along the fault at 2.0 s (Fig. 7d) is noticeable, which confirms the hypothesis that the failure of the weak shear layer along the fault plane and the shock-wave reflections from the Paleozoic layer contributed to favorable conditions for venting. On the west end the fault rupture due to large tensile stress patches is distinguished, and the cavity region is connected to the fault region and the top alluvial layer, which are under tension. This establishes the hypothesis that the venting was initiated because of the presence of the fault, the clay-rich tuff near

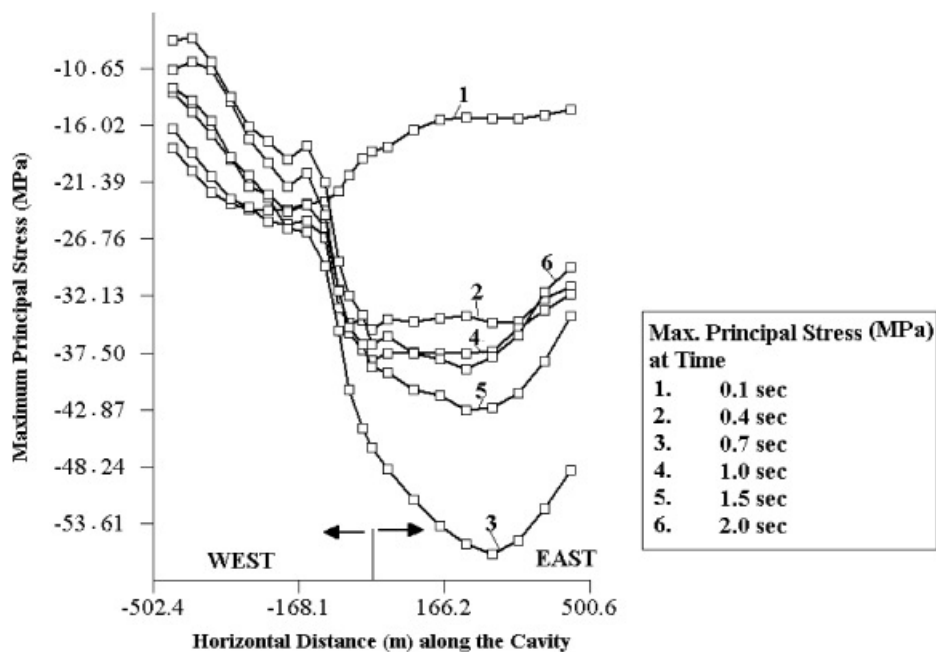


Fig. 8. Compressive principal stress field on east and west ends of the cavity along the horizontal grade for model 3.

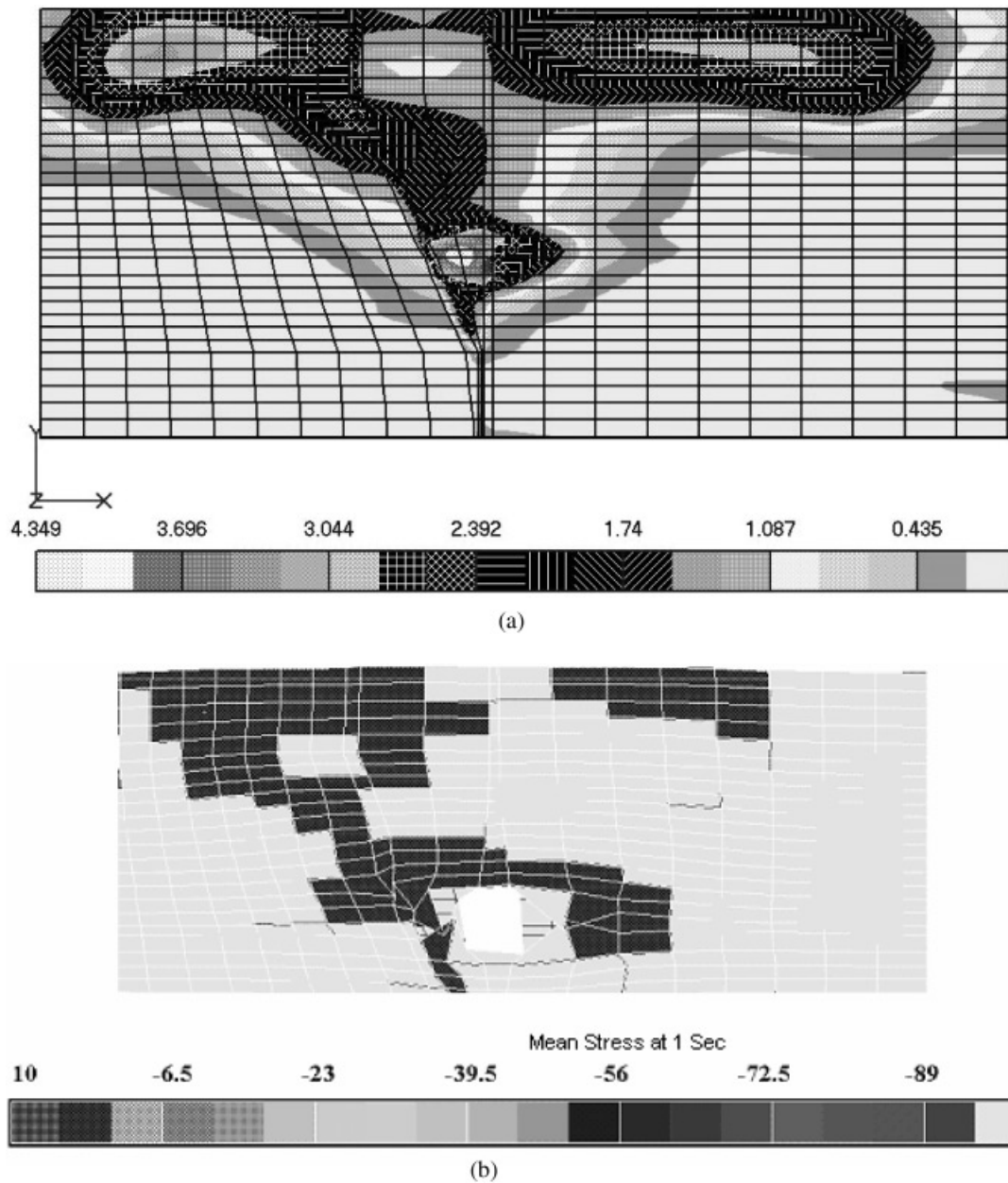


Fig. 9. At 1 s for model 3: (a) tensile strain (in percent) and (b) mean stress (in megapascals).

the cavity, and the closer Paleozoic layer underneath aggravating the situation by forming large tensile zones due to strong reflections.

Although in the alluvial region patches of tensile stresses at the free surface and near the tuff-alluvial interface are noticed, the cavity region is surrounded by the compressive stresses in the east end. The maximum compressive stress plot in Fig. 8 at the cavity elevation shows that on the east end the containment cage was relatively stronger compared to the west end. The tensile strain and the mean stress profiles are presented in Figs. 9a and 9b, respectively, at 1 s for model 3. The tensile strain level of

3 to 4% at the free surface is induced because of spall after the shock-wave reflection from GZ. Further, at this tensile strain level, with the interaction of the cavity with the ruptured fault and the tension-induced spall zone at GZ, the west end was more favorable for venting. In the east side spalled alluvial region, limited to the top alluvial free-surface zone, strain levels were relatively lower and resulted in contained behavior as is expected at this depth ( $SDOB \sim 129.3 \text{ m/kT}^{1/3}$ ). The nearly zero confinement shown with the mean stress profile of Fig. 9b clearly illustrates establishment of a vent path due to spall at the free surface and failure of the weaker shear

layers along the fault plane. The locations of zero mean stress on the west end near the cavity, around the fault plane on the west end, are consistent with the locations where radioactivity was identified in Terhune et al.'s<sup>2</sup> postshot drill experiments. Moreover, the predicted crack profile and the tensile strain of ~3% due to the event are found to be consistent with those observed by Terhune et al.<sup>1,2</sup>

A summary of results obtained from our computation is presented in Table XII, wherein a comparison with the field observations and Terhune et al.'s calculated results<sup>1,2</sup> is included. The present computational results are in excellent agreement with the previous computational work, which is available up to the short time duration of 1 s, and the measured field values for the crater profile observed after a longer duration.

**V. CONCLUSIONS**

The Baneberry event carried out on December 18, 1970, at the Nevada Test Site is a classic example that has all the complex geological features of a double-fault

system, variation of the geological strata, saturated tuff on the west end and clay-rich tuff on the east end across the fault plane, degraded Alluvium with high porosity closer to GZ, and an inclined hard Paleozoic layer underneath the source. This event has been successfully simulated by the 3-D finite element code SHOCK-3D in the present work. Terhune et al.<sup>1,2</sup> have concluded that all the undesirable features, namely, the closeness of the fault to the emplacement point, proximity of the hard Paleozoic layer underneath the source near the fault region on the west end, and the clay-rich tuff layer on the east end of the source formed an undesirable combination leading to venting, which is not expected with a large SDOB of 129.3 m/kT<sup>1/3</sup>.

At first the cavity growth closer to the existing Baneberry fault and fissures helped in easy passage of hot gases in the fault region. The weak shear zone in this region was easily ruptured from cavity-fault interaction. The strong shock reflection from the closer Paleozoic rock on the west end helped in forming a sliding mechanism along the fault plane. This sliding mechanism was also supported by the presence of 50% montmorillonite clay-rich tuff on the east end. This is a weaker material

TABLE XII  
Summary of Results and Comparison with Terhune et al.'s Earlier 2-D Computations and Site Observations\*

Comparison of Results up to 1 s				
Parameters	Observation <sup>a</sup>	BANE 1 Results <sup>a</sup>	BANE 2 Results <sup>a</sup>	Present Results
Cavity radius (m)	37.2	35 to 37	35 to 38	34 to 39
Peak particle velocity 140 m from the source (m/s)	11.0	9.0	8.0	8.9 to 9.5
Maximum spall velocity at GZ (m/s)	6.0	7.8	6.8	7.4 to 7.6
Maximum spall resultant displacement at GZ (m)	1.8	3.1	2.3	3.5 to 3.6
Maximum spall horizontal displacement leading to vent fissure at GZ (m)	1.0	1.0	Not available	0.8 to 0.9
Maximum failure strain (%)	—	>3	>3	>3
Additional Results and Comparisons				
Parameters	Observation <sup>a</sup>	Present Results		
Vent location	90 m southwest of source	97 m southwest of source		
Subsidence crater dimensions	24-m depth; 128-m diameter	20- to 35-m depth at 5- to 8-s duration Final subsidence zone of ~200-m diameter and 25- to 26-m depth stabilized quasi-static values.		
Maximum horizontal displacement after venting (m)	Not available	~3.3 to 3.4 m at vent location during the transient runs; ~8.5-m quasi-static value (qualitative prediction with model 4 for identifying vent location at GZ)		

\*References 1 and 2.

<sup>a</sup>Observation and BANE1 and BANE2 numerical results are from Terhune et al.<sup>1,2</sup>

compared to the partially saturated tuff on the west end. Thus, a dip-slip mechanism was formed, and the rock mass on the west end lifted up, causing rupture of the top alluvial layer leading to final venting.

The present 3-D integral analysis with SHOCK-3D enables more precise understanding of the failure behavior, and it has been demonstrated that the interaction of the weaker clay-rich tuff and the partially saturated tuff was, in fact, responsible for the formation of a sliding mechanism along the fault plane. This phenomenon, in addition to the aforementioned reasons for venting, is important, and the earlier reported axisymmetric models with inherent limitations could only approximately predict the failure mechanism. Thus, this study has helped to explain venting and final crater formation consistent with the site observations.

The comparative studies of the different models presented in this paper indicate that single- and double-fault models behave nearly the same during the transient duration. The extent of the fault in the strike direction does not strongly influence the venting behavior as compared to the friction offered by the weak shear layer strata within the fault plane. In fact, in model 4 with provision of full sliding along the fault, the liftoff and vent location could be accurately predicted. Model 3 shows a lift of comparatively lower order. Thus, from this parametric study it may be concluded that the shear zone marking the Baneberry fault was very weak. The in situ properties of the weak shear zone could be inferior to the weak clay material assumed in the analysis for model 3, and the presence of large voids and discontinuities is indicated. The present results show excellent comparison with the earlier predictions and field measurements of the Baneberry event and give us confidence in 3-D simulation capabilities for UNE events if site-specific field data are available.

## REFERENCES

1. R. W. TERHUNE, H. D. GLENN, D. E. BURTON, H. L. McKAGUE, and J. T. RAMBO, "Calculational Examination of the Baneberry Event," UCRL-52365, Lawrence Livermore Laboratory (1977).
2. R. W. TERHUNE, H. D. GLENN, D. E. BURTON, H. L. McKAGUE, and J. T. RAMBO, "Numerical Simulation of the Baneberry Event," *Nucl. Technol.*, **46**, 159 (1979).
3. J. F. SCHATZ, "Physics of SOC and TENSOR Code," UCRL-51352, 21, Lawrence Livermore Laboratory (Feb. 1973).
4. J. T. CHERRY and F. L. PETERSEN, "Numerical Simulation of Stress Wave Propagation from Underground Nuclear Explosions," IAEA-PL-388/15, pp. 241-325, "Peaceful Nuclear Explosions," International Atomic Energy Agency (1970).
5. J. F. SCHATZ, "SOC73, A One-Dimensional Wave Propagation Code for Rock Media," UCRL-51689, Lawrence Livermore Laboratory (Nov. 1974).
6. D. E. BURTON, C. M. SNELL, and J. B. BRYAN, "Computer Design of High-Explosive Experiments to Simulate Subsurface Nuclear Detonations," *Nucl. Technol.*, **26**, 65 (1975).
7. A. SOMMERFELD, *Partial Differential Equations in Physics*, Academic Press, New York (1949).
8. O. C. ZIENKIEWICZ, D. W. KELLY, and P. BETTESS, "The Sommerfeld (Radiation) Condition on Infinite Domains and Its Modeling in Numerical Procedures," C/R/302/77, University College of Swansea (1977).
9. O. C. ZIENKIEWICZ and R. L. TAYLOR, *The Finite Element Method*, 4th ed., chap. 11, McGraw-Hill Book Company, London (1991).
10. T. R. BUTKOVICH, "Gas Equation of State for Natural Materials," UCRL-14729, Lawrence Livermore Laboratory (Jan. 24, 1967).
11. T. R. BUTKOVICH, "Techniques for Generating Pressure-Volume Relationships and Failure Envelopes for Rocks," UCRL-51441, Lawrence Livermore Laboratory (Nov. 1973).
12. E. HOEK and E. T. BROWN, "Practical Estimates of Rock Mass Strength," *Int. J. Rock Mech. Min. Sci.*, **34**, 1165 (1998).
13. N. BICANIC and O. C. ZIENKIEWICZ, "Constitutive Model for Concrete Under Dynamic Loading," *Earthquake Eng. Structural Dynamics*, **11**, 689 (1973).
14. N. BICANIC, "Nonlinear Finite Element Transient Response of Concrete Structures," PhD Thesis, University of Wales (1978).
15. P. PERZYNA, "Fundamental Problems in Viscoplasticity," *Adv. Appl. Mech.*, **9**, 343 (1966).
16. N. CERVERA, E. HINTON, J. BONET, and N. BICANIC, "Nonlinear Transient Dynamic Analysis of Three Dimensional Structures—A Finite Element Program for Steel and Reinforced Concrete Structures," *Numerical Methods and Software for Dynamic Analysis of Plates and Shells*, Pineridge Press, Swansea, United Kingdom (1987).
17. N. CERVERA, E. HINTON, and O. HASSAN, "Nonlinear Analysis of Reinforced Concrete Plate and Shell Structured Using 20-Noded Isoparametric Brick Elements," *Comput. Structures*, **25**, 6, 845 (1987).
18. I. S. SANDLER, F. L. DiMAGGIO, and G. Y. BALADI, "Generalized Cap Model for Geological Materials," *ASCE J. Geo-Technical Div.* (July 1978).
19. S. E. YAMADA and A. S. ABOU-SAYEED, "Cap Model Guided by Energy Concept," *ASCE J. Geo-Technical Div.* (July 1978).
20. G. W. MA, H. HAO, and Y. X. ZHOU, "Modeling of Wave Propagation by Underground Explosion," *Computers Geophysics*, **22**, 3/4 (1998).